LANGMUIR

Article

pubs.acs.org/Langmuir

Exploiting the Marangoni Effect To Initiate Instabilities and Direct the Assembly of Liquid Metal Filaments

C. A. Hartnett,*[,†] I. Seric,[‡] K. Mahady,[§] L. Kondic,[‡] S. Afkhami,[‡] J. D. Fowlkes,[§,∥] and P. D. Rack[§,∥]

[†]Department of Physics & Astronomy, University of Tennessee, 1408 Circle Drive, Knoxville, Tennessee 37996, United States

[‡]Department of Mathematical Sciences, New Jersey Institute of Technology, Newark, New Jersey 07102, United States

[§]Department of Materials Science & Engineering, University of Tennessee, Knoxville, Tennessee 37996, United States

[∥]Center for Nanophase Materials Sciences, Nanofabrication Research Laboratory, Oak Ridge National Laboratory, Oak Ridge, Tennessee 37831, United States

Supporting Information

ABSTRACT: Utilization of the Marangoni effect in a liquid metal is investigated, focusing on initiating instabilities to direct material assembly via the Rayleigh−Plateau instability. Thin (2 nm) copper (Cu) films are lithographically patterned onto thick (12 nm) nickel (Ni) strips to induce a surface energy gradient at the maximum wavelength of the filament instability predicted by Rayleigh−Plateau instability analysis. The pattern is irradiated with an 18 ns pulsed laser such that the pattern melts and the resultant Ni−Cu surface tension gradient induces Marangoni flows due to the difference in surface energies. The experimental results, supported by extensive direct numerical simulations, demonstrate that the Marangoni flow exceeds the capillary flow induced by the initial geometry, guiding instabilities such that final nanoparticle location is directed toward the regions of higher surface energy (Ni regions). Our work shows a route for manipulation, by means of the Marangoni effect, to direct the evolution of the surface instabilities and the resulting pattern formation.

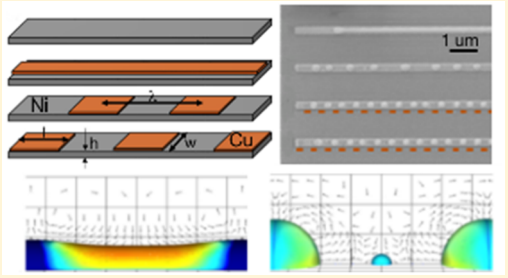

I. INTRODUCTION

Harnessing various intrinsic material properties and forces to achieve a directed assembly of nanostructures is one of the grand challenges of materials synthesis. Among the forces that are operative for materials assembly are those due to the Marangoni effect, material transport in response to a surface energy gradient. While classically observed in "wine tears",[1,2] Marangoni effects have seldom been exploited to direct materials assembly. Only recently have researchers demonstrated directed assembly of thin polymer films via photochemical patterning of the surface energy and photothermally generated surface energy gradients.[3−6] Of particular relevance to this paper, Bennett et al.[7] modeled Marangoni flow and resultant morphology in pulsed laser-treated Fe−P magnetic disk drives. Both thermocapillary forces induced by the pulsed laser profile and so-called chemicapillary forces induced by preferential phosphorus evaporation were considered. The resultant laser fluence-dependent morphologies could be accounted for via the combined thermocapillary and chemicapillary forces. In our work, we show how to guide surface instabilities using Marangoni effects due to the variation of material composition at the interface. The physical experiments are augmented by three-dimensional volume-of-fluid (VOF)-based simulations to provide a quantitative understanding of the Marangoni-induced mass transport at the interface.

Assembled metallic nanostructures have many applications, including photovoltaics,[8,9] enhanced Raman spectroscopy,[10,11] catalysis,[12] photonics,[13] plasmonics,[14] and spintronics.[15] Additionally, they are utilized in biodiagnostics where nanoparticle-based detection methods depend on coordination, size, and spacing.[16,17] Recently, pulsed laser-induced dewetting (PLiD) has been used in the self-assembly of metallic nanoparticles on a substrate.[18] In PLiD a thin film of metal is exposed to a 10−20 ns pulsed laser, sufficient to melt the metal on the time scale of 1 ns to tens of nanoseconds.[19] During the liquid lifetime extended thin films[19] or thin film strips/rings[20] undergo instabilities, and the resultant metallic nanoparticle assemblages possess correlated length scales. As we (and others) have shown, the natural spinodal instability (for 2-dimensional thin films) and Rayleigh−Plateau (RP) instability (for filaments) lead to dispersion in the particle size and spacing. Our focus is on understanding these fundamental instabilities and the governing hydrodynamics, and we explore ways to direct assembly for precise particle size and spacing to enable advanced functional nanoparticle arrays.

Directed assembly of liquid metal filaments has also been achieved by lithographically patterning sinusoidal perturbations

Received: May 23, 2017
Revised: July 18, 2017
Published: July 21, 2017

DOI: 10.1021/acs.langmuir.7b01655
Langmuir 2017, 33, 8123−8128

along the length of thin film strips (TFS).[21] Additionally, two-dimensional ordered arrays have been achieved by imposing perturbations in the thickness dimension via a 2-step thin film patterning process.[22] We explore a new approach, based on manipulating the surface energy along the length of a liquid metal filament during PLiD. The surface energy gradient leads to the transport of fluid from the regions of low surface energy to the regions of high surface energy as a result of the Marangoni effect. Our numerical simulations permit direct observation and characterization of flow, showing that the Marangoni effect due to the surface energy difference between Cu and Ni is initially the dominant force in driving the flow that controls the final location of the resulting nanoparticles. Since Cu has a lower surface energy than Ni we show that material flows toward the Ni region despite the competing effect caused by the capillary forces due to the initial geometry.

II. EXPERIMENTAL METHODS

To explore the composition-driven Marangoni flows we pattern thin rectangles of Cu on top of TFS of Ni, which are patterned on a thermally insulating supporting substrate of 100 nm SiO_2 on Si. The Ni−Cu system is chosen since it is an isomorphous system with complete solubility in the solid and liquid state; thus, secondary phase formation and reactions do not complicate the physics or mass transport. To achieve the Ni−Cu patterns a multiprocess electron beam lithography approach is used, utilizing a positive tone resist, polymethylmethacrylate (PMMA), and an e-beam current density of 900−1000 $\mu C/cm^2$. After resist development 12 ± 1 nm of Ni is deposited by dc magnetron sputtering. The pattern is then formed by standard lift-off procedures to generate the underlying Ni TFS, with widths of 185 and 370 nm. The nanofabrication steps are repeated to pattern 2 ± 1 nm thick Cu rectangular areas on top of the Ni. The spacing of the top Cu "perturbation" corresponds to the fastest growing wavelength predicted by the (linear) RP stability analysis, and the extent of the perturbation is one-half of the wavelength. According to RP analysis the stability of a jet is determined by its radius, R, such that the modes k for which $kR < 1$ are unstable and the modes for which $kR > 1$ are stable. Here, k is the wavenumber related to the perturbation wavelength by $k = 2\pi/\lambda$. The fastest growing mode corresponds to $k_mR \approx 0.7$. In the context of a TFS on the substrate, R corresponds to the radius of the filament of the same cross-sectional area as a TFS of thickness h, width w, and equilibrium contact angle θ: more precisely, $R = (hw/(\theta - \sin\theta\cos\theta))^{1/2}$.[23,24] At the filament thickness of $h = 12$ nm and the equilibrium contact angle of Ni in contact with SiO_2 of $\theta \approx 69°$, the radius of the filament is $R = 51$ and 71 nm for widths $w = 185$ and 370 nm, respectively. Hence, the fastest growing instability wavelengths in the experiments, $\lambda_{m,e} = 2\pi/k_{m,e}$, are 455 and 634 nm for $w = 185$ and 370 nm, respectively.

For comparison, each experiment includes a nonperturbed Ni TFS and a Ni TFS with a colinear Cu TFS with one-half of the Ni width patterned on it, equal to the same Cu volume per unit length as the spaced perturbation sample. Figure 1a is an illustration of the experimental setup and geometry. Figure 1b is a representative SEM image of a fabricated sample which shows (top-to-bottom) (i) pure Ni TFS, (ii) colinear Ni−Cu TFS, and (iii and iv) two Ni−Cu TFS with patterned Cu rectangular perturbations, one of which is simply phase shifted by one-half a wavelength relative to the other. Note that the Cu volume for ii is the same as that for iii and iv, since the Cu in ii is the full length of the Ni TFS but one-half the width, whereas the Cu in iii and iv is the full width of the Ni TFS but one-half of the total length. The differences in the results between i and iv will enable analyzing the Marangoni effect and its influence on instability development. Conveniently, there is adequate contrast in the secondary electron coefficients of Cu and Ni; the Cu appears darker and the Ni brighter in the as-synthesized patterned strips as evidenced in the secondary electron image, Figure 1b.

A krypton fluoride (KrF) excimer laser, wavelength 248 nm, energy range 250 ± 10 $mJ\cdot cm^{-2}$, and pulse width of 18 ± 2 ns fwhm, is used for PLiD. The liquid lifetime is dependent on the energy fluence delivered by a laser pulse and the thermal and optical properties of the Ni, the supporting SiO_2 layer, and the underlying Si substrate. The area of the laser spot is ∼1 cm^2, which is much larger than the ∼1 mm^2 area containing the patterned samples, thus ensuring a homogeneous fluence. Our simplified one-dimensional numerical simulation of the surface temperature of a 12 and 14 nm Ni TFS supported on 100 nm SiO_2 on Si and exposed to one laser pulse, at a fluence of 250 $mJ\cdot cm^{-2}$, reveals a 20 ns liquid lifetime and an average liquid metal temperature of 2313 and 2350 K, respectively.[23] The thin Cu pattern is also suspected to result in a slightly higher temperature and thus induce a small additional thermocapillary force. Future work will explore this effect, which is ignored in the present paper. Due to the finite liquid lifetime per laser pulse and rapid cooling, a series of individual laser pulses can be used to control the instability evolution and interrogate morphological changes of the liquid filament.[19]

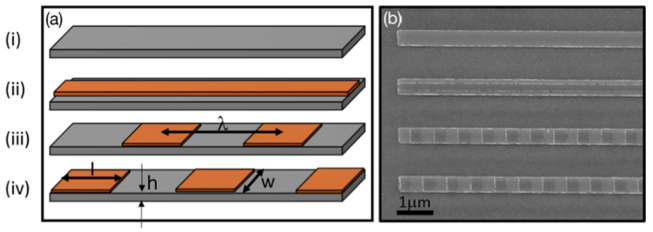

Figure 1. (a) Illustration and (b) SEM image of the experimental Ni−Cu thin film strip (TFS) geometry setup: (i) 12 nm thick (h) Ni strip (various widths (w) explored); (ii) 12 nm thick Ni strip with a 2 nm Cu strip patterned on top along the centerline but one-half the width of the Ni strip; (iii) 12 nm thick Ni strip with 2 nm Cu rectangles patterned at a wavelength (λ) with the same width as the Ni but only one-half of the wavelength length (l); (iii) similar to iv; however, the Cu pattern is phase shifted by one-half a wavelength (i.e., Cu in pattern iv is aligned with Ni-only regions in strip iii).

III. COMPUTATIONAL METHODS

The experimental results are supported by direct numerical simulations based on a volume-of-fluid (VOF) method.[25,26] The liquid metal filament is modeled as an isothermal, incompressible Newtonian fluid using the Navier−Stokes equations

$$\rho\frac{D\mathbf{u}}{Dt} = -\nabla p + \nabla\cdot(\mu(\nabla\mathbf{u} + \nabla\mathbf{u}^T)) + \kappa\sigma\delta_s\mathbf{n} + \nabla_s\sigma\delta_s \quad (1)$$

$$\nabla\cdot\mathbf{u} = 0 \quad (2)$$

where D/Dt is the material derivative, velocity field $\mathbf{u} = (u,v,w)$, pressure p, curvature of the fluid−vapor interface κ, and the normal vector at the fluid−vapor interface $\delta_s\mathbf{n}$, where δ_s is the surface delta function.[27] The term $\nabla_s\sigma$ represents the surface gradient of the surface energy, which depends on the concentration of Ni and Cu at the interface; the alloy composition value of surface energy is defined as the weighted algebraic average of the pure material surface energies, given below. The material species are advected with the flow according to $Dc_i/Dt = 0$, where c_i is the material concentration and i = Cu, Ni. Since advection is expected to be dominant, as discussed further below, we do not consider diffusive effects. The concentrations are initialized according to the experimental geometry. In order to model the fluctuations existing in fabrication of the experimental initial geometry we perturb the initial height of the filament by random noise of the form $h_r = \sum_i^N a_i\cos(i\pi x/4\lambda_m)$ with a constraint that $|h_r| < 1$ nm, a_i are random amplitudes taken from a uniform distribution, and $N = 125$. We show the results for four realizations of random noise. In the simulations, due to the limitations of the present simulation setup, we use a contact angle of 90°, resulting in R smaller compared to the experimental setup, i.e., $R = 37.6$ and 53.2 nm for filament widths of $w = 185$ and 370 nm, respectively. Hence, the spacing of the Cu perturbations in the simulations corresponding to the fastest growing mode are $\lambda_{m,s} = 340$ and 477 nm for $w = 185$ and 370 nm, respectively.

DOI: 10.1021/acs.langmuir.7b01655
Langmuir 2017, 33, 8123−8128

The boundary condition for the in-plane velocities on the substrate is the Navier-slip boundary condition $(u,w)|_{y=0} = \beta\partial_y(u,w)|_{y=0}$, where (u,w) are the in-plane components of the velocity[28] and β = 20 nm denotes the slip length; note, y points out of the plane of the substrate and x along the filament.[29]

The equations are solved using the open source flow solver Gerris[30] with interface tracking based on the VOF method, extended with the computations of the surface gradients of the surface tension at the interface, $\nabla_s\sigma$.[38] The interface is tracked implicitly by introducing a volume fraction function, χ, which gives the fraction of the liquid phase in each computational cell. The viscosity, μ, and density, ρ, depend on the volume fraction by $\mu = \chi\mu_l + (1-\chi)\mu_v$ and $\rho = \chi\rho_l + (1-\chi)\rho_v$, where the subscripts l and v denote the liquid and vapor phases. For computational efficiency and to minimize the effect of the surrounding vapor (i.e., air), we set $\mu_v = \mu_l/20$ and $\rho_v = \rho_l/20$; the factor of 20 is sufficiently large to ensure that its exact value is not important. To confirm that this is the case, we carried out additional simulations with the factor of 100 and found that the only effect of this larger value is slightly faster (1 − 2 ns) breakup. Furthermore, we assume the values of ρ_l and μ_l are that of Ni at the melting temperature for both the Cu and the Ni regions. The spatial discretization is accomplished using an adaptive mesh, with the resolution close to the fluid−vapor interface being ∼1.5 nm.

Before closing this section, we briefly comment on the relative importance of diffusive and advective effects. An extrapolation of the Cu self-diffusion coefficient (D) at the Ni melting temperature results in a diffusion coefficient of $\sim 6 \times 10^{-9}$ m^2/s.[31] Thus an estimate of the diffusion distance, $(4Dt)^{1/2}$, where t is the liquid lifetime and D is assumed to be constant at the Ni melting temperature, yields ≈ 22 nm. The results of simulations show that advection leads to complete coverage by Cu (therefore, Cu covers the distance of ∼100 nm) in approximately 1/3 of the liquid lifetime. We conclude that advection effects are dominant, justifying ignoring diffusive effects in the simulation results that follow. The fact that the time scale of relevance to convective effects is short compared to the liquid lifetime suggests that the Marangoni effect is considerable, particularly during the beginning of the first laser pulse by "kick starting" the instability development.

IV. RESULTS

Before presenting the experimental and simulation results for the patterned Ni−Cu setup it is instructive to first illustrate the geometric influence that 2 nm of additional Ni material has on instability evolution and final nanoparticle placement. Figure 2 shows a simulation of a Ni TFS with w = 185 nm, h = 12 nm, and an additional 2 nm of Ni patterned on top along the TFS length at a perturbation spacing corresponding to the fastest growing simulation wavelength, $\lambda_{m,s}$. The material parameters for density, viscosity, and surface energy are those at the Ni melting temperature (1728 K), 7810 kg·m^{-3}, 4.9 mPa·s, and 1.78 N·m^{-1}, respectively. The following purely geometric effects are observed: (1) following the melting by the laser, patterned 2 nm regions generate peaks in the height profile and troughs in the unpatterned regions, producing a filament height perturbation; (2) as the filament evolves, the troughs propagate toward the substrate since the wavelengths are unstable with respect to RP type of instability; (3) eventually the filament breaks up and the resultant nanoparticles are positioned at the peak locations where the original 2 nm of additional Ni material was patterned. We note formation of small secondary (satellite) drops between the large primary ones; we will discuss this finding in more detail later in the text.

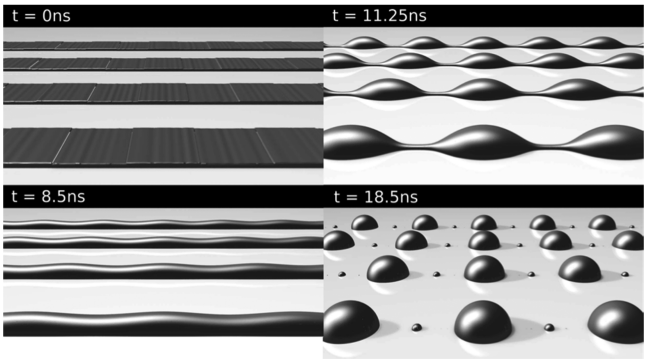

Figure 2. Simulation snapshots of the Ni−Ni TFS geometry; underlying Ni TFS is 12 nm thick and 185 nm in width, with an additional 2 nm Ni perturbation on top, 170 nm in length, and a wavelength of 340 nm.

With this context, we demonstrate that patterned Ni−Cu setups evolve quite differently due to the Marangoni effect. The surface energy of Cu at the Ni melting temperature (1.24 N·m^{-1})[32] is lower than that of Ni (1.77 N·m^{-1}),[33,34] a difference of 0.53 N·m^{-1}. Thus, during PLiD, if the Marangoni effect is operative and dominant it should induce material flow from the thicker patterned Cu region to the adjacent Ni region and ultimately generate a surface perturbation such that the resultant nanoparticles are located in the initially thinner Ni-only regions.

Figure 3 shows the results for the TFS geometry with w = 185 nm; Figure 3a shows the overlay of the original pattern and the resulting configuration after a single laser pulse, and Figure 3b is an overlay of the original pattern and the resulting configuration after 5 laser pulses, where (i) pure Ni TFS, (ii) colinear Ni−Cu TFS with Cu width of 93 nm, (iii and iv) Ni TFS with Cu rectangular perturbations with spacing corresponding to $\lambda_{m,e}$ = 455 nm, and length of 224 nm (the dashed lines below iii and iv denote the initial patterned Cu areas). It is very clear in the single laser pulse image in Figure 3a that

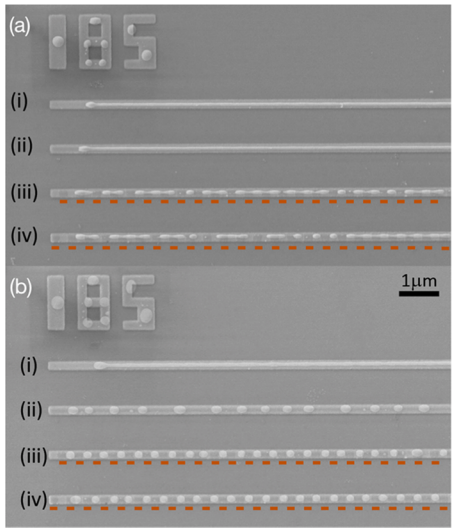

Figure 3. Experimental PLiD results for the Ni−Cu TFS geometry, 185 nm in width and 12 nm thick, after (a) one and (b) five lasers pulses at a fluence of 250 mJ·cm^{-2}: (i) pure Ni TFS, (ii) colinear Ni−Cu TFS, 2 nm thick Cu and 93 nm in width; (iii and iv) Ni−Cu TFS geometries with patterned Cu rectangular perturbations, 2 nm thick, 224 nm in length, with a wavelength of 455 nm, that of the fastest growing instability, and the pattern in iv is shifted relative to iii by one-half a pattern wavelength—the dashes under strips iii and iv indicate the location of the patterned Cu and is added for clarity.

DOI: 10.1021/acs.langmuir.7b01655
Langmuir 2017, 33, 8123−8128

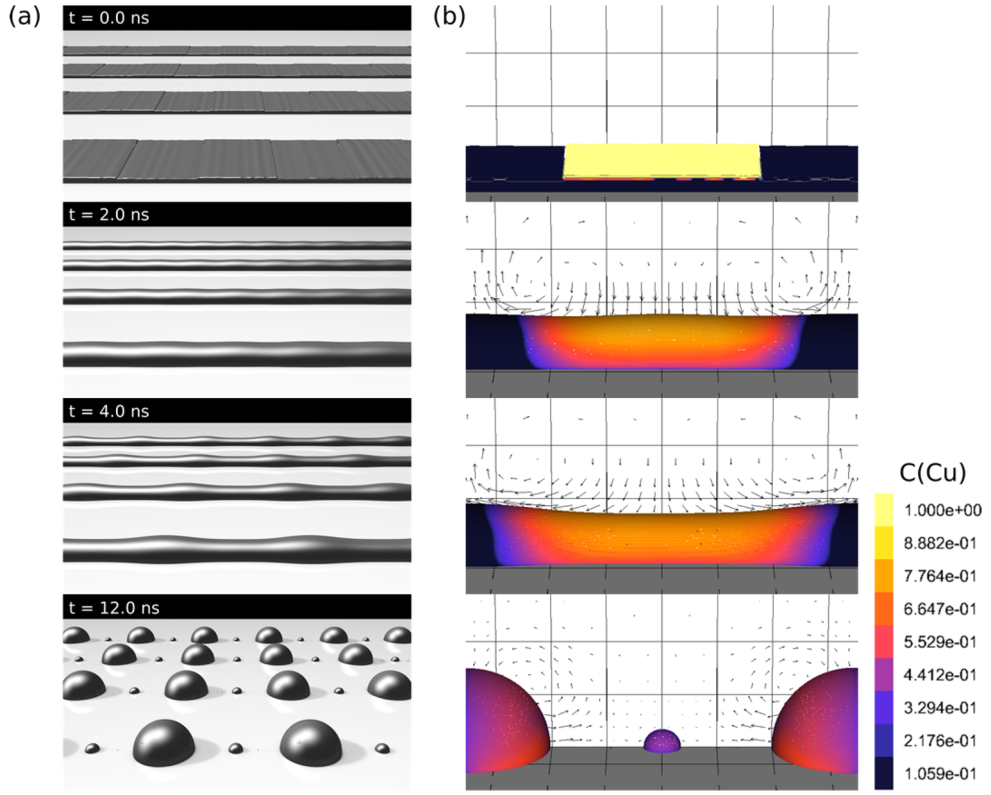

Figure 4. Ni−Cu TFS geometry simulation snapshots; underlying Ni TFS is 12 nm thick and 185 nm in width: (a) Collection of four independent simulations, Cu perturbations are 2 nm thick and 170 nm in length with a wavelength of 340 nm, RP predicted unstable filament wavelength; (b) close up of a over one perturbation wavelength showing one-half of the filament width with the color representing the concentration of Cu at the interface and the vector field representing the velocity field at the cross section along the axis of the symmetry of the filament.

pattern inversion occurred in iii and iv for the patterned Cu perturbations geometries, whereas the instability development is much slower for the pure Ni TFS (i) and the colinear Ni−Cu strip (ii). The five laser pulse image in Figure 3b (iii and iv) shows that the perturbations have grown until pinch off and nanoparticle formation occurs, with very good spatial fidelity corresponding to the original Ni-only regions. Interestingly, breakup occurs randomly and at longer wavelengths in ii, and little if any instability growth is observed in i, where contraction of the filament can be observed instead (see Diez et al.).[35] Particle spacing in i and ii was expected to mimic the RP instability dispersion curve for Ni and Ni−Cu filaments suspended on SiO_2.[36]

Spatial correlation analysis of Figure 3a (iii and iv) reveals a wavelength of 446 nm, which is very close to the patterned target of 455 nm. Analyses of the location of the nanoparticles using a spatial correlation function shows a dominant particle−particle spacing of 475 nm, which is also in good agreement with the patterned Cu perturbation spacing. Some particle shifting is observed which is likely due to small inconsistencies in the pinch-off time and subsequent transport along the axial direction and toward any regions not yet pinched off. A similar coarsening was observed in simulations and experiments of Cu rings on SiO_2.[20] Additional supporting experimental results for a 370 nm width Ni−Cu TFS sample can be found in the Supporting Information.

We next present the results of numerical simulations. Figure 4 illustrates the time evolution of a Ni−Cu TFS geometry with w = 185 nm and Cu perturbations corresponding to setups iii and iv shown in Figure 2. TFS spacing corresponds to $\lambda_{m,s}$ found in simulations (as a reminder, since simulations use a 90° contact angle, λ_m = 340 nm). Figure 4a shows the evolution of four filaments with random noise. Figure 4b shows the close up of the simulation over one wavelength of the perturbation; the colors represent the concentration of Cu at the interface. The vector field represents the fluid velocity field at the cross section along the axis of symmetry of the filament. At t = 2 ns we can see from the velocity field that the Marangoni effect drives the fluid away from the Cu regions toward the adjacent Ni areas. At t = 4 ns the perturbation locations are clearly inverting to the Ni regions. The filament continues to evolve with time, driven by the RP instability, eventually breaking into nanoparticles.

As noted previously, one feature of the simulation results is the formation of small secondary (satellite) particles that form in between the large primary ones, see Figures 2 and 4. While secondary particles could be also seen in the experimental images, in particular, Figure 3b (ii−iv), the appearance and placement of secondary particles are much more regular in the simulations. We previously investigated hierarchical secondary (and tertiary) particle formation for geometrically defined sinusoidal perturbations.[37] The mechanisms leading to secondary particles for the Marangoni-induced perturbations are not yet known, and we leave further discussion of this issue to future work.

To explore the effect that the pattern wavelength has on the pattern formation a variety of wavelengths were patterned, including the ones characterized by positive growth rates (unstable) and negative growth rates (stable). Table 1 lists the relevant wavelengths, and Figure 5a−e illustrates the series of as-synthesized TFS, and resultant pattern formation after a

DOI: 10.1021/acs.langmuir.7b01655
Langmuir 2017, 33, 8123−8128

Table 1. Stability Properties as the Wavelength of Perturbation Is Varied[a]

kR	wavelength (λ) (nm)	comment
0.2	1587	smallest unstable growth rate
0.4	794	similar growth rate as kR = 0.9
0.7	455	max growth rate
0.9	353	similar growth rate as kR = 0.4
1.1	289	stable wavelength

[a]Estimated R of 185 nm wide and 12 nm thick filament radius = 51 nm.

single laser pulse is given in Figure 5f–j. As commented, the instability growth rate increases for kR values of 0.2–0.7, peaking at 0.7, and then decreasing for 0.9 (which is comparable to 0.4), followed by 1.1 that is stable. After 1 laser pulse, the filament geometry has been "frozen" in, but careful examination of the perturbations that have developed along the filaments reveal interesting information about the perturbation growth rates. To better illustrate the perturbation evolution Figure 5k–o gives cropped and magnified images of the bottom filament (denoted by the dashed box) in images Figure 5f–j, respectively.

As can be seen in Figure 5f–j, the amplitudes of the resultant instabilities are consistent with the expected instability growth rates. First, the peak growth rate of kR = 0.7 appears to have the highest amplitude. Second, the roughly equivalent kR = 0.4 and 0.9 growth rates have lower amplitudes but reproduce the periodicity of the patterned Cu. The slow developing unstable growth rate kR = 0.2 pattern has disperse varicose perturbation wavelength distribution and not representative of the original large wavelength values. Finally, the stable kR = 1.1 pattern does seem to form perturbations at the unstable wavelength, with an albeit very small amplitude. Interestingly, after 5 pulses (see Supporting Information) these perturbations appear to have not grown or possibly decayed which is consistent with our previous studies using geometrically patterned sinusoidal perturbations.[21,23]

To conclude this section, we also consider in the VOF simulations the setup that should be stable with respect to the RP type of instability. Figure 6 shows a filament evolution,

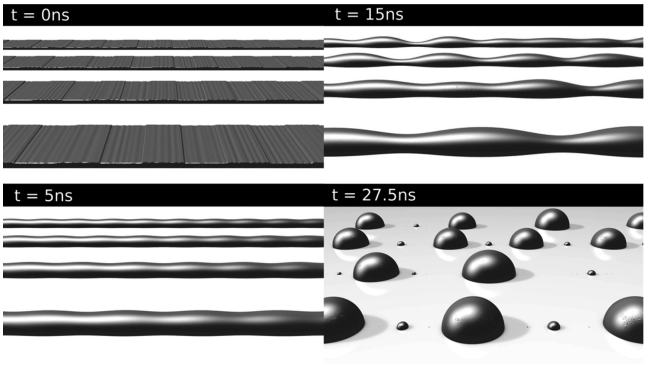

Figure 6. Ni–Cu TFS geometry simulation snapshots; underlying Ni TFS is 12 nm thick and 185 nm in width, Cu perturbations are 2 nm thick, 91 nm in length with a wavelength of 182 nm, which is a stable filament wavelength according to RP analysis. Note that the final particle distribution differs from the imposed pattern.

width w = 185 nm and Cu perturbation spacing of 182 nm, corresponding to kR = 1.1. At t = 5 ns we can see the emergence of the inverted perturbation forming, which is consistent with the Marangoni-induced transport of material from the Cu to the Ni regions. However, at longer times (15 ns) this initial perturbation decays and new longer wavelengths have formed, consistent with the RP stability criteria. Eventually the filament breaks into nanoparticles with two primary nanoparticles per computational domain, corresponding to a spacing of 364 nm. Therefore, as expected, perturbing TFS with wavelengths that are stable with respect to the RP stability analysis does not lead to the formation of particle assemblies conforming to the wavelength of imposed perturbations.

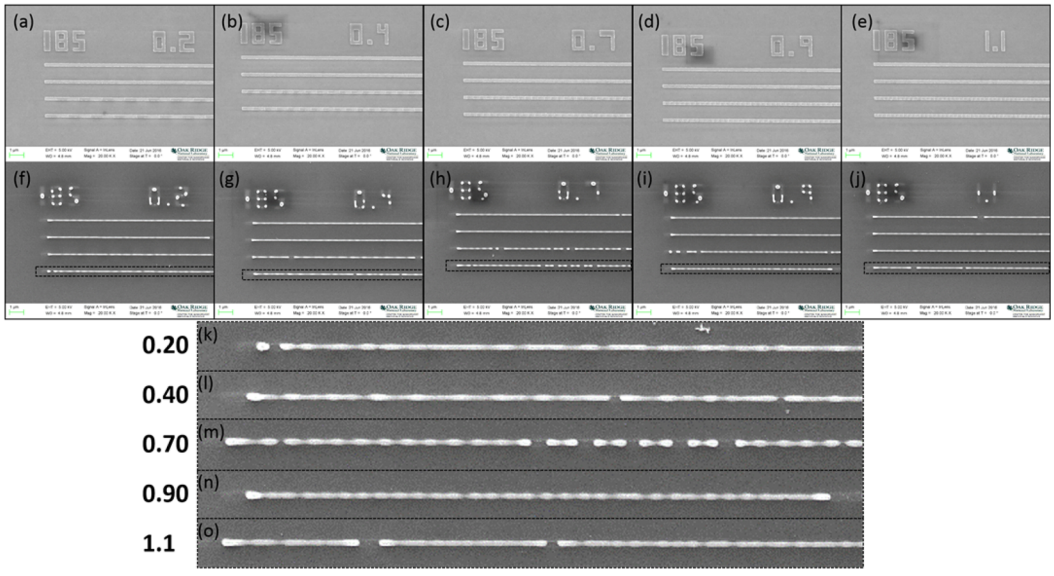

Figure 5. Scanning electron micrograph of as-synthesized (a–e) and after a single laser pulse (f–j) pattern with various wavelengths with different RP instability growth rates. (k–o) Cropped and magnified images of the bottom filaments (note dashed regions) in f–j and correspond to kR values of 0.2, 0.4, 0.7, 0.9, and 1.1, respectively (see Table 1).

DOI: 10.1021/acs.langmuir.7b01655
Langmuir 2017, 33, 8123–8128

V. SUMMARY

To date, the directed assembly of metallic nanostructures using PLiD has focused on imparting instabilities by lithographically patterning geometric perturbations to direct the ordering of resultant nanoparticles. Here we investigate a new approach to imparting instabilities by templating the surface energy by selectively patterning the surface of Ni thin films strips with Cu, where the patterning length scales were selected as the wavelengths of maximum growth rate predicted by the Rayleigh−Plateau stability analysis. Experimental results are confirmed and rationalized via fully nonlinear 3D simulations using a VOF method that includes the spatially varying surface energy. The patterned Cu regions have a lower surface energy than the Ni regions and induce Marangoni flow. Future work will explore applications of a similar approach to directed assembly for other relevant geometries.

■ ASSOCIATED CONTENT

Supporting Information

The Supporting Information is available free of charge on the ACS Publications website at DOI: 10.1021/acs.langmuir.7b01655.

Two additional experimental results: Ni−Cu TFS geometry, 12 nm thick, width w = 370 nm, Cu patterned at fastest growth rate wavelength 634 nm, single laser pulse 250 mJ·cm^{-2}; Ni−Cu TFS geometry, 12 nm thick, width w = 185 nm, Cu patterned at stable wavelength 289 nm, single laser pulse 250 mJ·cm^{-2} (PDF)

■ AUTHOR INFORMATION

Corresponding Author

*E-mail: chartnet@vols.utk.edu.

ORCID

C. A. Hartnett: 0000-0002-2363-3041

Notes

The authors declare no competing financial interest.

■ ACKNOWLEDGMENTS

The authors acknowledge support from the collaborative NSF CBET Grants 1603780 and 1604351. Sample preparation (lithography and metal deposition) were conducted at the Center for Nanophase Materials Sciences, which is a DOE Office of Science User Facility.

■ REFERENCES

(1) Gennes, P.-G. d.; Brochard-Wyart, F. o.; Quéré, D. *Capillarity and wetting phenomena: drops, bubbles, pearls, waves*; Springer: New York, 2004; p xv, 291 p.

(2) Thomson, J. *Philos. Mag. Ser. 4* **1855**, *10*, 330−333.

(3) Arshad, T. A.; Kim, C. B.; Prisco, N. A.; Katzenstein, J. M.; Janes, D. W.; Bonnecaze, R. T.; Ellison, C. J. *Soft Matter* **2014**, *10*, 8043−8050.

(4) Katzenstein, J. M.; Janes, D. W.; Cushen, J. D.; Hira, N. B.; McGuffin, D. L.; Prisco, N. A.; Ellison, C. J. *ACS Macro Lett.* **2012**, *1*, 1150−1154.

(5) Favazza, C.; Trice, J.; Kalyanaraman, R.; Sureshkumar, R. *Appl. Phys. Lett.* **2007**, *91*, 043105.

(6) Singer, J. P.; Kooi, S. E.; Thomas, E. L. *J. Polym. Sci., Part B: Polym. Phys.* **2016**, *54*, 225−236.

(7) Bennett, T. D.; Krajnovich, D. J.; Grigoropoulos, C. P.; Baumgart, P.; Tam, A. C. Marangoni Mechanism in Pulsed Laser Texturing of Magnetic Disk Substrates. *J. Heat Transfer* **1997**, *119*, 589−596.

(8) Atwater, H. A.; Polman, A. *Nat. Mater.* **2010**, *9*, 205−213.

(9) Wu, J. L.; Chen, F. C.; Hsiao, Y. S.; Chien, F. C.; Chen, P. L.; Kuo, C. H.; Huang, M. H.; Hsu, C. S. *ACS Nano* **2011**, *5*, 959−967.

(10) Anker, J. N.; Hall, W. P.; Lyandres, O.; Shah, N. C.; Zhao, J.; Van Duyne, R. P. *Nat. Mater.* **2008**, *7*, 442−453.

(11) Vo-Dinh, T. *TrAC, Trends Anal. Chem.* **1998**, *17*, 557−582.

(12) Christopher, P.; Xin, H. L.; Linic, S. *Nat. Chem.* **2011**, *3*, 467−472.

(13) Ozbay, E. *Science* **2006**, *311*, 189−193.

(14) Halas, N. J.; Lal, S.; Chang, W. S.; Link, S.; Nordlander, P. *Chem. Rev.* **2011**, *111*, 3913−3961.

(15) Wolf, S. A.; Awschalom, D. D.; Buhrman, R. A.; Daughton, J. M.; von Molnar, S.; Roukes, M. L.; Chtchelkanova, A. Y.; Treger, D. M. *Science* **2001**, *294*, 1488−1495.

(16) Rosi, N. L.; Mirkin, C. A. *Chem. Rev.* **2005**, *105*, 1547−1562.

(17) Le, F.; Brandl, D. W.; Urzhumov, Y. A.; Wang, H.; Kundu, J.; Halas, N. J.; Aizpurua, J.; Nordlander, P. *ACS Nano* **2008**, *2*, 707−718.

(18) Trice, J.; Thomas, D.; Favazza, C.; Sureshkumar, R.; Kalyanaraman, R. *Phys. Rev. B: Condens. Matter Mater. Phys.* **2007**, *75*, 235439.

(19) Favazza, C.; Kalyanaraman, R.; Sureshkumar, R. *Nanotechnology* **2006**, *17*, 4229−4234.

(20) Wu, Y.; Fowlkes, J. D.; Roberts, N. A.; Diez, J. A.; Kondic, L.; Gonzalez, A. G.; Rack, P. D. *Langmuir* **2011**, *27*, 13314−13323.

(21) Fowlkes, J. D.; Kondic, L.; Diez, J. A.; González, A. G.; Wu, Y.; Roberts, N. A.; McCold, C. E.; Rack, P. D. *Nanoscale* **2012**, *4*, 7376−7382.

(22) Wu, Y. Y.; Dong, N. Y.; Fu, S. F.; Fowlkes, J. D.; Kondic, L.; Vincenti, M. A.; de Ceglia, D.; Rack, P. D. *ACS Appl. Mater. Interfaces* **2014**, *6*, 5835−5843.

(23) Fowlkes, J. D.; Kondic, L.; Diez, J.; Wu, Y. Y.; Rack, P. D. *Nano Lett.* **2011**, *11*, 2478−2485.

(24) Rayleigh, L. *Proceedings of the London Mathematical Society* **1878**, *s1−10*, 4−13.

(25) Mahady, K.; Afkhami, S.; Kondic, L. *J. Comput. Phys.* **2015**, *294*, 243−257.

(26) Hirt, C. W.; Nichols, B. D. *J. Comput. Phys.* **1981**, *39*, 201−225.

(27) Zemach, C. *J. Comput. Phys.* **1992**, *100*, 335−354.

(28) Mahady, K.; Afkhami, S.; Diez, J.; Kondic, L. *Phys. Fluids* **2013**, *25*, 112103.

(29) Hartnett, C. A.; Mahady, K.; Fowlkes, J. D.; Afkhami, S.; Kondic, L.; Rack, P. D. *Langmuir* **2015**, *31*, 13609−13617.

(30) Popinet, S. *J. Comput. Phys.* **2009**, *228*, 5838−5866.

(31) Meyer, A. *Phys. Rev. B: Condens. Matter Mater. Phys.* **2010**, *81*, 012102.

(32) Matsumoto, T.; Fujii, H.; Ueda, T.; Kamai, M.; Nogi, K. *Meas. Sci. Technol.* **2005**, *16*, 432.

(33) Brillo, J.; Egry, I. *J. Mater. Sci.* **2005**, *40*, 2213−2216.

(34) Gale, W. F.; Totemeier, T. C. *Smithells metals reference book*; Butterworth-Heinemann, 2003.

(35) Diez, J. A.; Gonzalez, A. G.; Kondic, L. *Phys. Fluids* **2009**, *21*, 082105.

(36) Kondic, L.; Diez, J. A.; Rack, P. D.; Guan, Y. F.; Fowlkes, J. D. *Phys. Rev. E* **2009**, *79*, 026302.

(37) Fowlkes, J. D.; Roberts, N. A.; Wu, Y.; Diez, J. A.; Gonzalez, A. G.; Hartnett, C.; Mahady, K.; Afkhami, S.; Kondic, L.; Rack, P. D. *Nano Lett.* **2014**, *14*, 774−782.

(38) Seric, I.; Afkhami, S.; Kondic, L. Direct numerical simulation of variable surface tension flows using a Volume-of-Fluid method; https://arxiv.org/abs/1703.00327; 2017.

DOI: 10.1021/acs.langmuir.7b01655
Langmuir 2017, 33, 8123−8128